On the measurement and interpretation of the fluxes of galactic cosmic-ray nuclei

Ferronato Bueno, Eduardo

DOI:
10.33612/diss.253636377

7. Measurement of the deuteron flux in cosmic rays with the AMS-02 experiment

The methods needed for measuring the $Z = 1$ isotopic fluxes in cosmic rays were presented in the past three chapters. In chapter 4, an estimator for cleaning the sample and easing mass separation was built, followed, in chapter 5, by a parametric inverse mass template fit method used for isotopic identification, already incorporating fragmentation corrections and systematic uncertainties. Chapter 6 presented an unfolding method used to deconvolute the measured spectrum from instrumental effects.

We now build on the developed methods to obtain the isotopic fluxes as a function of the kinetic energy per nucleon and rigidity. We start by recalling that the flux of a particle as a function of the variable x in the bin i is defined as

$$\Phi(x_i) = \frac{N(x_i)}{\delta(x_i)A(x_i)\Delta T \Delta x_i}\,, \tag{7.1}$$

where N is the number of events, δ the data/simulation efficiency corrections presented in chapter 6, A the acceptance including the total selection efficiency, ΔT the exposure time, and Δx_i the bin width.

In this chapter, the measurement of the deuteron flux in cosmic rays will be presented, using ten years of AMS-02 data, from May 2011 to May 2021. The first six sections are devoted to deriving each term in equation 7.1, in the following order: bin width, exposure time, efficiency corrections, acceptance and the number of events. In section 7, the estimation of the systematic uncertainties associated with the flux measurements is presented. In section 8, the final isotopic flux measurements are shown as a function of the kinetic energy per nucleon and rigidity. Section 9 uses the results to obtain the secondary-to-primary ratios d/p and d/^{4}He, and the secondary-to-secondary ratio d/^{3}He. They are then compared to the models obtained in chapters 2 and 3. Section 10 summarizes and concludes.

7.1 The choice of the binning

As already discussed in previous chapters, the identification of isotopes in AMS-02 is performed by using the mass of the particle, which is calculated by combining the measurements of the rigidity, R, and of the velocity, β, according to the equation

$$m = \frac{RZe}{\beta\gamma}\,, \tag{7.2}$$

where Ze is the magnitude of the charge, and γ is the Lorentz factor. This dependence on R and β makes it possible to bin the data in any of these two variables. The choice of the variable then comes from the resolution of each measurement: the tracker measures the rigidity with a resolution of $\approx 10\%$ up to 20 GV[1], whereas the TOF measures the velocity with a resolution $\sigma_\beta/\beta \approx 4\%$ for particles with $\beta = 1$ and $Z = 1$ [2]. In the same conditions, the RICH-NaF has a velocity resolution of approximately 0.35%, while the RICH-AGL has a resolution of 0.12% [3]. Considering these numbers, binning the data in velocity is advantageous because the better resolution allows for thinner bins, which eases the identification of the particles as the phase-space of the mass is reduced. These three subdetectors are used to measure the velocity in overlapping ranges:

1. **TOF:** $0.5 < \beta < 0.9$
2. **RICH-NAF:** $0.78 < \beta < 0.99$
3. **RICH-AGL:** $0.96 < \beta < 0.997$

The isotopic fluxes measured as a function of the velocity are usually presented as a function of the kinetic energy per nucleon $E_k = (\gamma - 1)m_p$, where γ is the Lorentz factor. However, some of the physical processes at play, such as diffusion and the solar modulation, are rigidity dependent [4]. Thus, providing the measurements as a function of R is also of interest to the astroparticle physics community. Using the same binning as the one used by the AMS collaboration in the measurement of the ^{4}He flux [5] is interesting because it allows for the calculation of the d/^{4}He ratio using the published AMS-02 results. As discussed in chapter 1, this ratio is relevant for propagation and solar modulation studies.

Considering equation 7.2, it is possible to build a velocity binning for a given particle mass m that corresponds to the chosen rigidity binning. Hence, in this work, the binning is defined starting from the rigidity binning of the ^{4}He flux measurement by AMS-02 [5]. We start with a set of rigidity bins given at the publication:

$$\{R_i\} = \{R_0, R_1, ..., R_n\}\,, \tag{7.3}$$

which are then converted to velocity using equation 7.2

$$\{\beta(m)_i\} = \{\beta_0(m), \beta_1(m), ..., \beta_n(m)\}\,. \tag{7.4}$$

In this analysis, however, we identify protons and deuterons, which have different masses. Figure 7.1 shows the curves of rigidity versus velocity for both particles, highlighting how differently the velocity evolves with R in

each case. Therefore two sets of velocity bins are built: one assuming that $m = m_p$, and another assuming $m = m_d$, where m_p and m_d are the proton and deuteron masses, respectively. These velocity scales built directly from the R bins do not yet take advantage of the resolution of the velocity measurements. Thus, subdivisions are created according to the velocity resolution of each detector, with the number of subdivisions being

$$n = \frac{\beta_{j+1} - \beta_j}{\sigma_\beta}\,, \tag{7.5}$$

where β_j and β_{j+1} correspond to the original bin edges directly converted from the rigidity binning, and σ_β is the velocity resolution. The width of each interval is then $\Delta\beta = (\beta_{j+1} - \beta_j)/n$. If the division $(\beta_{j+1} - \beta_j)/\sigma_\beta$ is not a natural number, n is rounded and the width of the last bin is simply $\beta_n - \Delta\beta$, where β_n is the last bin edge as defined in equation 7.4. Since AMS-02 measures the velocity with three different subdetectors, the velocity bins are built following this method for each detector.

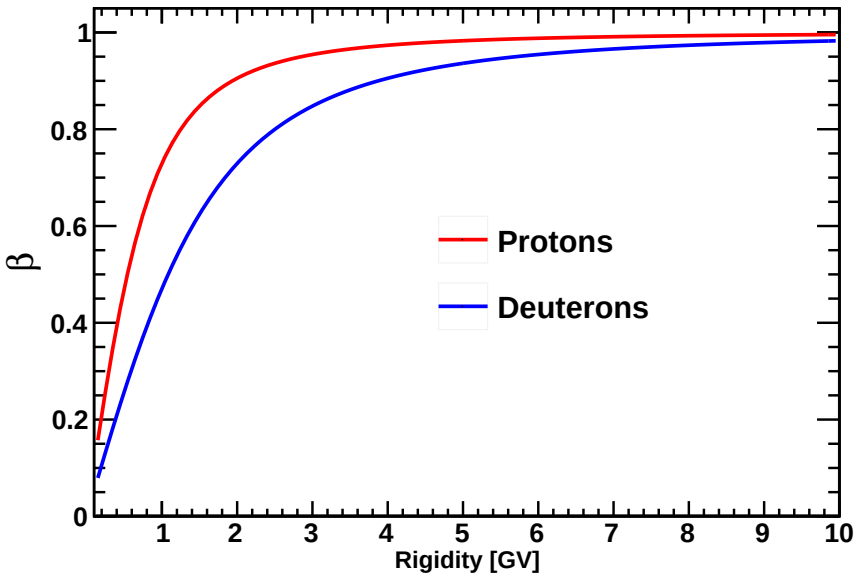

Figure 7.1: Velocity as a function of rigidity for protons (red) and deuterons (blue).

The choice of the binning in velocity also affects how the exposure time is computed, as is discussed in greater detail in the next section.

7.2 Geomagnetic cutoff and exposure time

After their journey through the interstellar medium (ISM) and the Heliosphere, CRs must overcome one last obstacle before being detected by AMS-02: the magnetosphere of the Earth [6]. When particles traverse this region, their trajectory is modified depending on their rigidity. Below a specific value, called cutoff rigidity, the trajectory cannot be extrapolated to outside the magnetosphere [7], implying that particles below this threshold value are from atmospheric origin. To ensure that the particles are indeed galactic CRs, the events must have a rigidity above the cutoff rigidity at the geomagnetic location in which they were detected. The cutoff rigidity is determined using the most recent IGRF model [8].

However, it is essential to remember that the events are binned in velocity. As seen in equation 7.2, deuterons have twice the rigidity of protons in a given velocity bin. Therefore, the sample would be biased if such selection was applied at rigidities close to the cutoff value. To circumvent this problem, knowing that there are two bin sets, one for protons and one for deuterons, the cutoff selection is applied as a function of the velocity: each cutoff rigidity value, R_C, is converted to velocity, assuming the mass m of the particle:

$$\beta_C(m) = \frac{R_C}{\sqrt{m^2 + R_C^2}}\,. \tag{7.6}$$

Therefore, in each set of bins, the mass of the respective particle is assumed, and a velocity cutoff is calculated. The event is then accepted if the following condition is satisfied:

$$\beta > (1 + 2\sigma_\beta)\beta_C\,, \tag{7.7}$$

where β is the measured velocity, and σ_β the velocity resolution of the detector (TOF, NAF or AGL). The factor $1 + 2\sigma_\beta$ is what is called a *safety factor* [9]: to avoid selecting particles with atmospheric origin simply due to velocity resolution effects, the measured velocity has to be larger than the cutoff value by a factor equal to two times the resolution of the detector measuring the velocity. Although the number of events is reduced, this enhances the purity of the sample.

The geomagnetic cutoff selection affects the exposure time, as it prevents particles below a certain velocity from being measured in a given geomagnetic location. In AMS-02, the detector live time corresponds to

the fraction of a one-second gate in which the trigger was not busy, thus ready for detection. The exposure time is then given by the sum of the live time in the data period being analyzed. Due to the applied cutoff velocity selection, the exposure time depends on three items:

1. **Particle type:** deuterons have a higher mass, therefore for a given cutoff rigidity, β_C is lower as seen in figure 7.1, leading to a higher exposure time.
2. **Velocity:** the higher the velocity of the particle, the more likely it is to be above the cutoff, increasing the exposure time.
3. **Detector:** a safety factor dependent on the resolution of the subdetector is used for the cutoff selection. Thus, the detector with better resolution will have more events for the same velocity. Therefore the AGL has a larger exposure time than the NAF, which, in turn, is larger than the one from the TOF.

The exposure time is computed by summing the live time for all bins above the cutoff; for a given β_C value, all bins with lower edge satisfying the condition 7.7, are incremented by Δt, the live time of the detector in that second. Figure 7.2 shows the exposure time in seconds for both protons and deuterons in the three different ranges, where all the effects listed are seen.

It is important to stress that the dependence of the exposure time on the mass of the particle must be treated with care: for the same value of R_C, we have $\beta_C(m_p) > \beta_C(m_d)$. As protons are faster than deuterons, a fraction of the atmospheric protons will satisfy the condition $\beta > \beta_C(m_d)$, leading to an atmospheric proton population in the sample selected with the deuteron cutoff velocity. Hence, in this data sample, only deuterons are counted as they are the only particles that are ensured to be of galactic origin. In the case where $\beta_C(m_p)$ is used for the cutoff selection, this problem does not exist as no atmospheric deuteron will be able to satisfy the condition $\beta > \beta_C(m_p)$. Hence, both protons and deuterons are of galactic origin, meaning that both particles can be counted. However, as deuterons are slower, their number is lower if compared to the other sample. Thus, by using different cutoff velocities, we can optimize the number of events of both species.

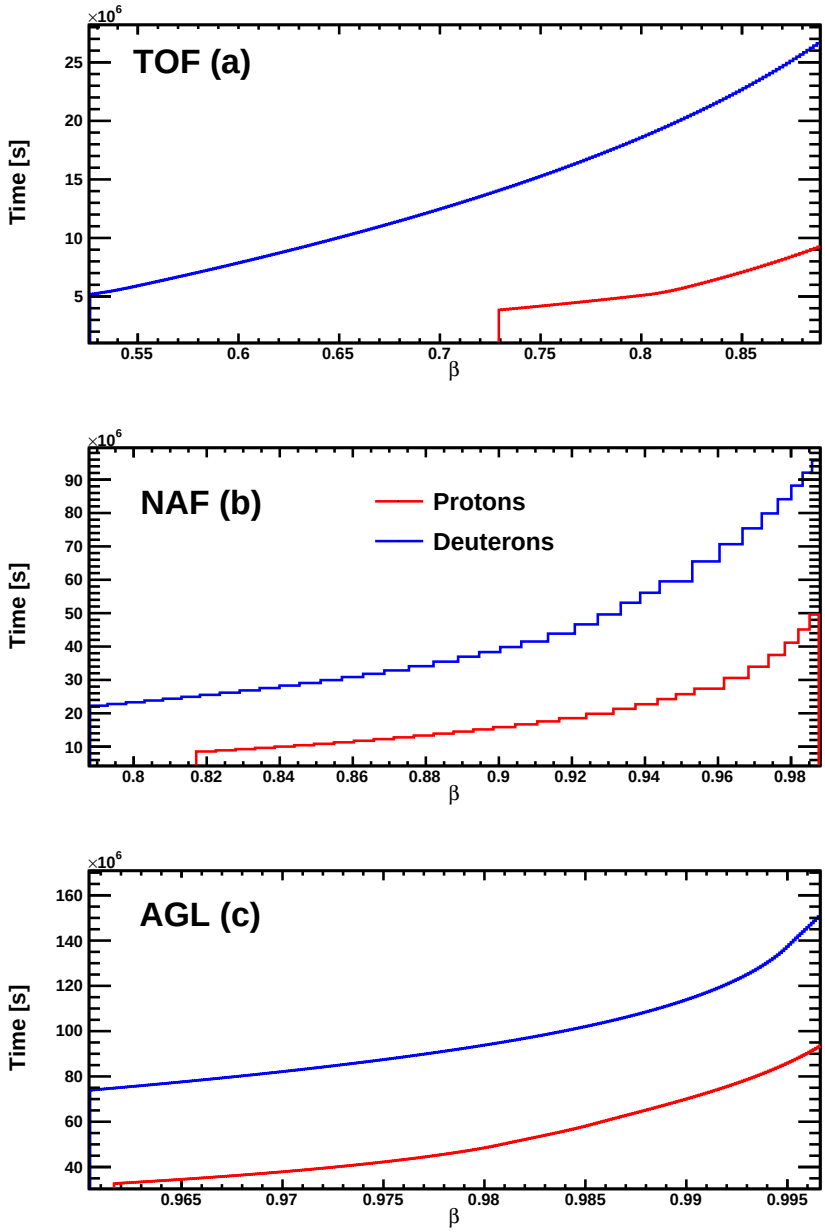

Figure 7.2: Exposure time as a function of the reconstructed velocity β for protons (red) and deuterons (blue), in the TOF (a), NAF (b), and AGL (c).

7.3 Event selection

After the analysis bins are defined, and the geomagnetic cutoff selection is applied, the events are selected according to the physics goals of the analysis. In the case of singly-charged isotopes, there are three main groups[1] of selection criteria that must be applied:

1. **Single-charge:** since this analysis focuses on single-charged particles, the tracker and the TOF are used to ensure that the charge Z of the events is compatible with 1 in different positions of the detector, from the top of AMS-02 to the lower TOF.
2. **Quality of the rigidity:** as the mass reconstruction depends on the rigidity, several criteria are applied to ensure the quality of the reconstructed track.
3. **Quality of the velocity:** analogously to the case of the rigidity, the events are only selected if they have met the minimum required for a good velocity reconstruction in the TOF and the RICH (in the case of measurements performed by the NaF and the AGL).

In addition, a trigger selection is applied to ensure that the trigger signal at the time of detection is compatible with a physical event (the details of the trigger logic are presented in appendix 7.A). The details of each criteria group are discussed below.

7.3.1 Single-charge selection

As discussed in chapter 5, one of the primary sources of background in the identification of singly-charged isotopes is the fragmentation of higher Z nuclei, which may leave spurious $Z = 1$ signals. In order to mitigate this effect, the redundancy of the measurement of the electric charge in different stages of the detector was used.

A cut on the charge of the first layer of the tracker ensures that the particles entering AMS-02 are singly-charged. The cut is applied using the highest available signal on the first layer. The charge is calculated based on the strongest energy-loss signal detected by the first layer, ensuring that heavier particles are rejected. More precisely, the criterion is $0.8 < Z_{L1} < 1.6$. Given the finite resolution of this charge measurement, the charge is verified further in the detector, namely in the TOF and the inner tracker (layers from 2 to 8, inside the magnetic field). The cut on the TOF charge is applied in the two independent pairs of layers, that is, in the lower TOF, where $0.75 < Z_{LTOF} < 1.3$, and in the upper TOF, where

[1] Although more selection criteria are applied, these are the most relevant and were chosen to be discussed for conciseness.

$0.75 < Z_{UTOF} < 1.5$. A cut is also applied on the charge measured by the inner tracker, $0.75 < Z_{Inner} < 1.5$, where all the layers used to reconstruct the track are used to compute the charge. Note that the tighter selection on the lower TOF is related to the removal of the interactions as discussed in chapter 4.

7.3.2 Tracker quality selection

Several selection criteria are applied to the data to ensure the quality of the reconstructed track and, therefore, the rigidity. First, only events with a single reconstructed track are allowed to reduce the number of events with spurious hits. Moreover, this track must be inside the fiducial volume of the inner tracker, have a hit on layer 2, right above the magnet, and hits in at least one layer of each remaining pair inside the magnetic field (layers 3 to 8). Writing in terms of the boolean operators AND (&&) and OR ($\|$), the hit pattern is

$$L2 \;\&\&\; (L3 \| L4) \;\&\&\; (L5 \| L6) \;\&\&\; (L7 \| L8)\,. \tag{7.8}$$

Additionally, to ensure the quality of the reconstructed track, events are required to have χ^2/NDF of the track fitting procedure below 10 in both the bending (y) and non-bending (x) coordinates, as explained in chapter 1.

7.3.3 Velocity quality selection

The velocity is measured by the TOF and the RICH detectors, with the latter having two radiator materials. The selection criteria applied to TOF variables are used in the whole data sample. In contrast, the RICH has its specific set of quality cuts for each radiator. Hence, the data sample of each RICH radiator has its specific set of cuts. The TOF selection requires that events have used the four layers of scintillators to reconstruct the velocity. Additionally, the fitting of the velocity using the information of the tracker yields two variables: χ^2_C and χ^2_T, which represent the chi-squared of the fit in the coordinates and time, respectively. Both these values are required to be below 10.

As discussed in chapter 4, interactions taking place inside AMS-02 produce secondary particles that can affect the reconstruction of the Cherenkov ring. As explained in that chapter, the ring quality selection is based of the following quality criteria: at least 3 PMTs used in the reconstruction, at least 40% of the detected photons used in the

reconstruction, and a maximum difference of 5% between the TOF and RICH velocity reconstructions. In addition, a cut is applied to the Boosted Decision Tree estimator presented in the same chapter, requiring it to be above 0.05 in the AGL, and above 0.1 in the NAF.

A summary of the criteria applied in each selection block is shown in table 7.1. In the next section, the efficiency of these groups of criteria will be calculated.

Selection block	Selection applied
Single-charge	$0.8 < Z_{L1} < 1.6$
	$0.75 < Z_{LTOF} < 1.5$
	$0.75 < Z_{UTOF} < 1.3$
	$0.75 < Z_{Inner} < 1.3$
Rigidity quality	Single-track
	Track inside fiducial volume
	Track hit pattern
	$\chi^2_{X,Y}/NDF < 10$
Velocity (TOF)	4 scintillator planes used
	$\chi^2_{C,T}/NDF < 10$
Velocity (RICH)	RICH BDT selection
	At least 3 PMTs
	At least 40% of detected photons
	used in the reconstruction
	RICH/TOF velocity matching

Table 7.1: Summary of selection criteria used in the three major selection stages of this measurement.

7.4 Efficiencies and corrections

As described in chapter 6, the efficiencies of the selection criteria are estimated from the simulations as a function of the true variable. In addition, they must be corrected due to possible data/simulation discrepancies, which can only be estimated as a function of the measured variable. Hence, this leads us to the expression

$$\varepsilon(x_i) \rightarrow \varepsilon(x_t) \underbrace{\prod_k \frac{\varepsilon_{Data}(x_m^k)}{\varepsilon_{MC}(x_m^k)}}_{\delta(x_m)}, \tag{7.9}$$

where ε_{MC} and ε_{Data} are, respectively, efficiencies as estimated from simulations and experimental data for the set (k) of data selection criteria, x_t is the true variable, x_m is the measured one, and $\delta(x_m)$ are the so-called data/simulation corrections.

The determination of the efficiencies is a procedure that requires care, as there might be correlations between selection criteria. Consequently, the efficiency evaluation samples must be constructed to avoid any biases. Two samples are needed for the evaluation of $\varepsilon(x_i)$ for a criterion (or group of criteria): the base sample, which consists of a data set with some selection criteria that do not correlate with the criteria being evaluated and a selected sample, which consists of the base sample with the addition of the selection criteria being evaluated. The ratio between the number of events in the selected sample and the base sample is, therefore, the efficiency of the selection. This process is done for data and simulations, allowing the calculation of $\delta(x_m)$. These efficiencies are calculated as a function of the natural logarithm of the rigidity. This choice is because a cubic spline function is adjusted to the points to have a smooth description of $\delta(x_m)$, thus minimizing the effects of statistical fluctuations. The use of the logarithm of the rigidity eases this parametrization as it spreads the points at low rigidity, making fewer knots necessary.

Two examples of calculations are given: one for the quality of the rigidity and the other for the velocity in the RICH and the TOF. The efficiencies in both data and simulations are shown, as well as the ratio between them with the spline fit and the respective uncertainty band. Since the $Z = 1$ sample in experimental data is constituted mainly by protons, this comparison is made with simulated proton events.

7.4.1 Quality of the rigidity

In this case, the base sample is selected by requiring that the events have a physical trigger and that the charge of the TOF and tracker (L1 and inner tracker) is compatible with one. Additionally, the TOF quality cuts are applied. The selected sample consists of the base sample with the addition of the cuts described in section 7.3.2.

Table 7.2 summarizes the criteria for both samples. The results are shown in figure 7.3, where the efficiency of this selection is shown for both data and simulated events in the top panel, while in the bottom, the ratio is shown together with the spline fit and the 95% C. L. band. The efficiency grows as a function of the rigidity of the particle as they are less likely to interact with AMS material. The ratio shows a good agreement between data and simulations (within 1%) in the whole range.

Data sample	Selection applied
Base sample	Physical trigger Good TOF charge Good tracker charge Good TOF reconstruction
Selected sample	Base sample selection Tracker quality selection

Table 7.2: Sample definition for the calculation of the efficiency of the tracker quality selection.

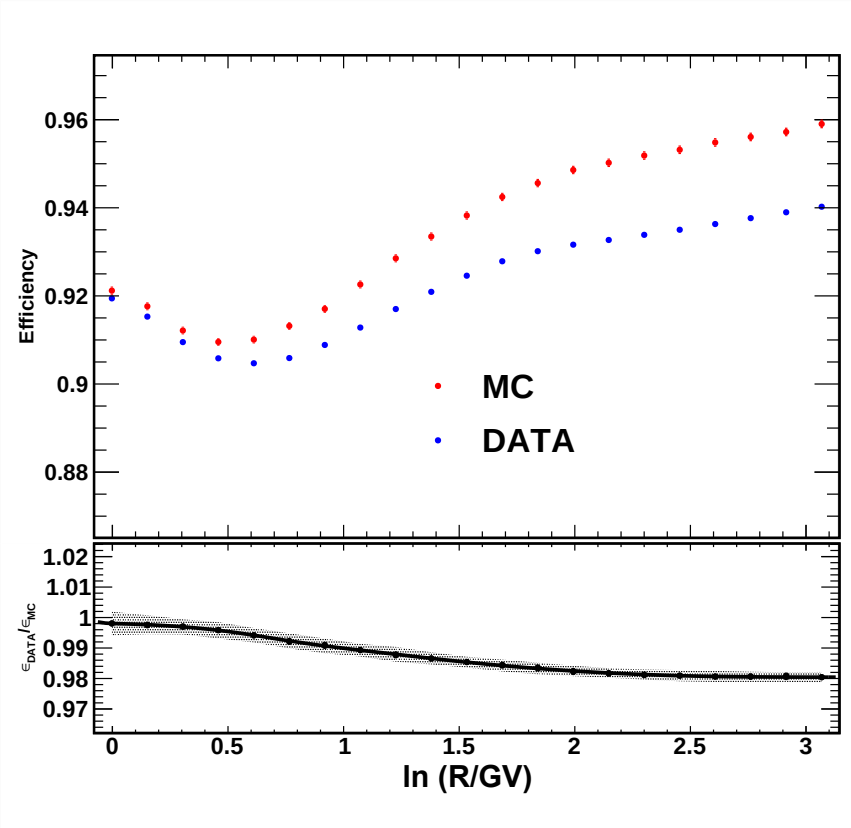

Figure 7.3: The top panel shows the tracker quality criteria efficiency in data (blue) and simulations (red) as a function of $ln(R)$, with their statistical uncertainties. The bottom panel shows the data/simulation ratio together with the spline fit and the 95% C. L. band.

7.4.2 Quality of the velocity

Since two different subdetectors measure the velocity, the efficiency is also calculated separately for the TOF and for the RICH.

7.4.2.1 TOF

The base sample in the TOF consists of events with a good trigger, good charge selection in the tracker (L1 and inner) and the TOF, and a good track reconstruction. The selected sample adds the quality cuts described in section 7.3.3. Table 7.3 summarizes the criteria applied in both samples for calculating this efficiency. The results are shown in figure 7.4 for both data and simulations. As seen, the efficiency of this selection is very high in both data and simulations, which have an agreement better than 1% in the whole range.

Data sample	Selection applied
Base sample	Physical trigger Good TOF charge Good tracker charge Good tracker reconstruction
Selected sample	Base sample TOF quality selection

Table 7.3: Sample definition for the calculation of the efficiency of the TOF quality selection

7.4.2.2 RICH

In the case of the RICH, the base sample consists of events with good trigger, charge, rigidity and velocity reconstruction in the TOF. The selected sample contains the criteria specific to the RICH described in section 7.3.3. Table 7.4 summarizes the selection criteria in both samples. Figure 7.5a shows the results for the NAF range. The efficiency is lower close to the threshold, increasing to a maximum, then decreasing with rigidity. This effect is also seen in the AGL, shown in figure 7.5b. This is because the Cherenkov rings increase with the velocity, becoming harder to reconstruct. Data and simulations differ significantly in both cases, with the simulations underestimating the background, stressing the importance of calculating the data/simulation corrections.

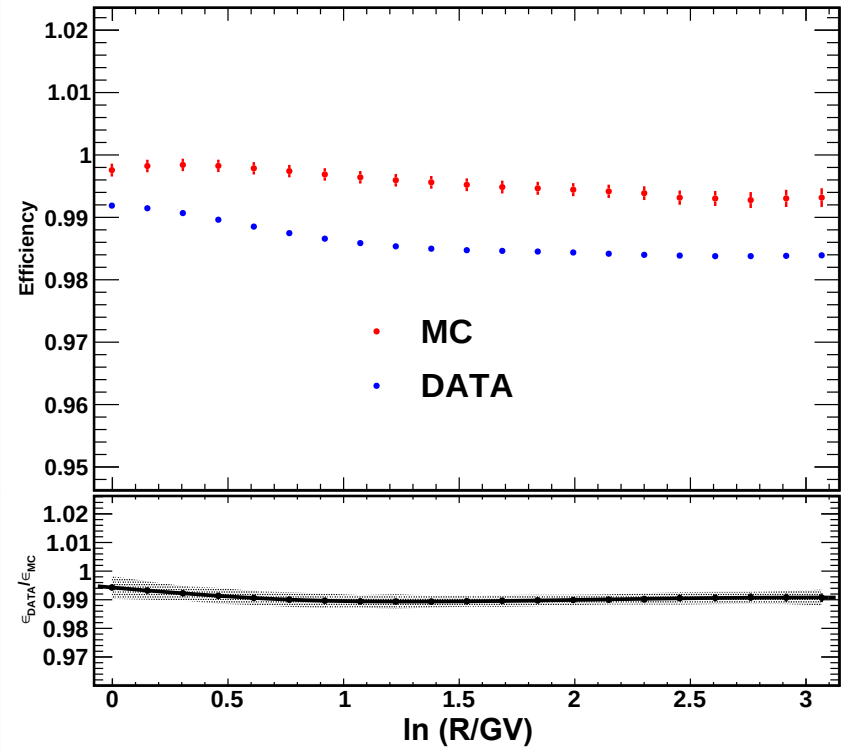

Figure 7.4: he top panel shows the TOF quality criteria efficiency in data (blue) and simulations (red) as a function of $ln(R)$, with their statistical uncertainties. The bottom panel shows the data/simulation ratio together with the spline fit and the 95% C. L. band.

Data sample	Selection applied
Base sample	Physical trigger
	Good TOF charge
	Good tracker charge
	Good tracker reconstruction
	Good TOF reconstruction
Selected sample	Base sample
	RICH quality selection

Table 7.4: Sample definition for the calculation of the efficiency of the RICH quality selection.

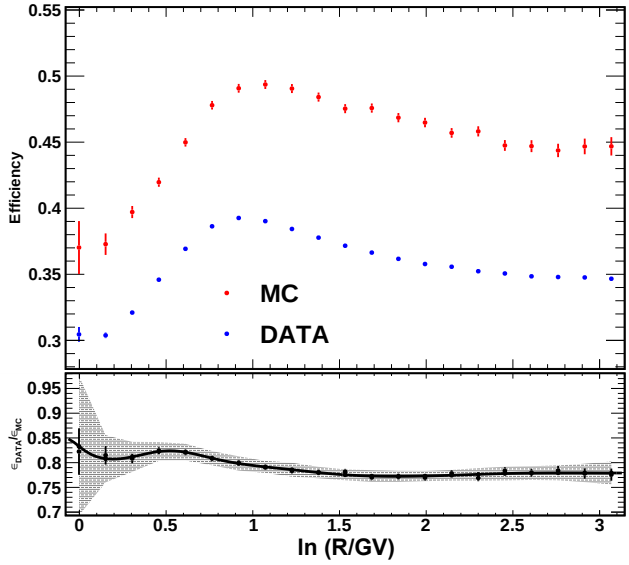

(a)

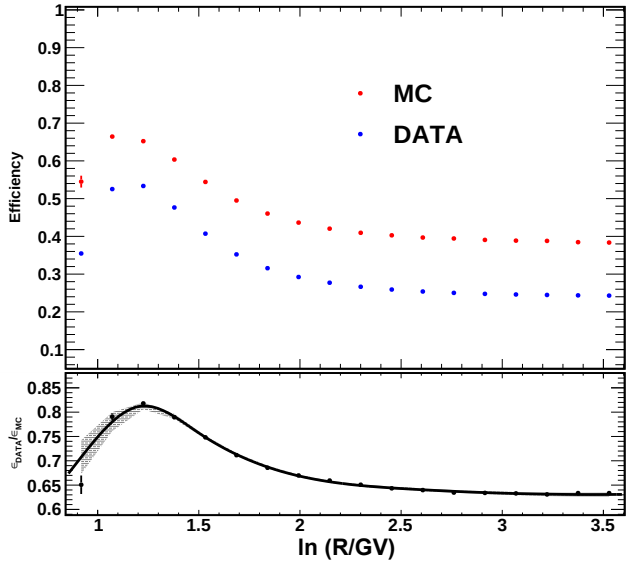

(b)

Figure 7.5: Efficiency of the RICH quality selection in the NAF (a) and AGL (b). In both cases, the top panel shows the efficiency in data (blue) and simulations (red) as a function of $ln(R)$, with their statistical uncertainties. The bottom panels shows the data/simulation ratio together with the spline fit and the 95% C. L. band.

7.4.3 Total corrections

The total data/simulation corrections are obtained by calculating the product of all groups of selection criteria as in equation 7.9. Panels (a), (b) and (c) of figure 7.6 show the total efficiency corrections as a function of the kinetic energy per nucleon in the TOF, NAF and AGL, respectively. The conversion between $ln(R)$ and kinetic energy was done by using the spline fits, assuming the mass of either a proton or a deuteron. However, RICH efficiencies require caution as they depend on the velocity, especially near the Cherenkov emission threshold. As we are comparing protons in the data and simulations, the proton mass is assumed even for deuterons in these cases. The displayed uncertainties correspond to the propagation of the uncertainties from each spline fit.

The results show that significant corrections are needed, especially in the RICH range, increasing near the Cherenkov emission threshold. This indicates that the simulations are underestimating the background present in the data and reinforces the necessity of applying such corrections.

The following section will describe the calculation of the acceptance, incorporating the total selection efficiency.

7.5 Acceptance

The AMS-02 detector simulations are generated assuming an isotropic flux above the detector. The flux is generated from a plane above the instrument, with dimensions 3.9×3.9 m^2, covering the whole field of view. The geometric acceptance for the generation plane, A_{top}, is then given by

$$A_{top} = \int_{S,\Omega} d\vec{S} \cdot d\vec{\omega} = l^2\pi \approx 47.78 \text{ m}^2\text{sr}\,, \tag{7.10}$$

where dS and $d\omega$ are the elements of the surface S and of the solid angle Ω, respectively. The geometric acceptance differs from A_{top} for a given analysis due to the selection efficiency. In this analysis, for instance, the events must traverse AMS-02 from the first layer of the tracker to the RICH radiator plane, thus reducing the geometrical acceptance. Therefore, the true geometric acceptance of the analysis, which already incorporates the total selection efficiency, is given by the ratio between the number of events generated in the simulation, N_{gen}, and the number of events passing the selection, N_{sel}, multiplied by generation acceptance, A_{top}:

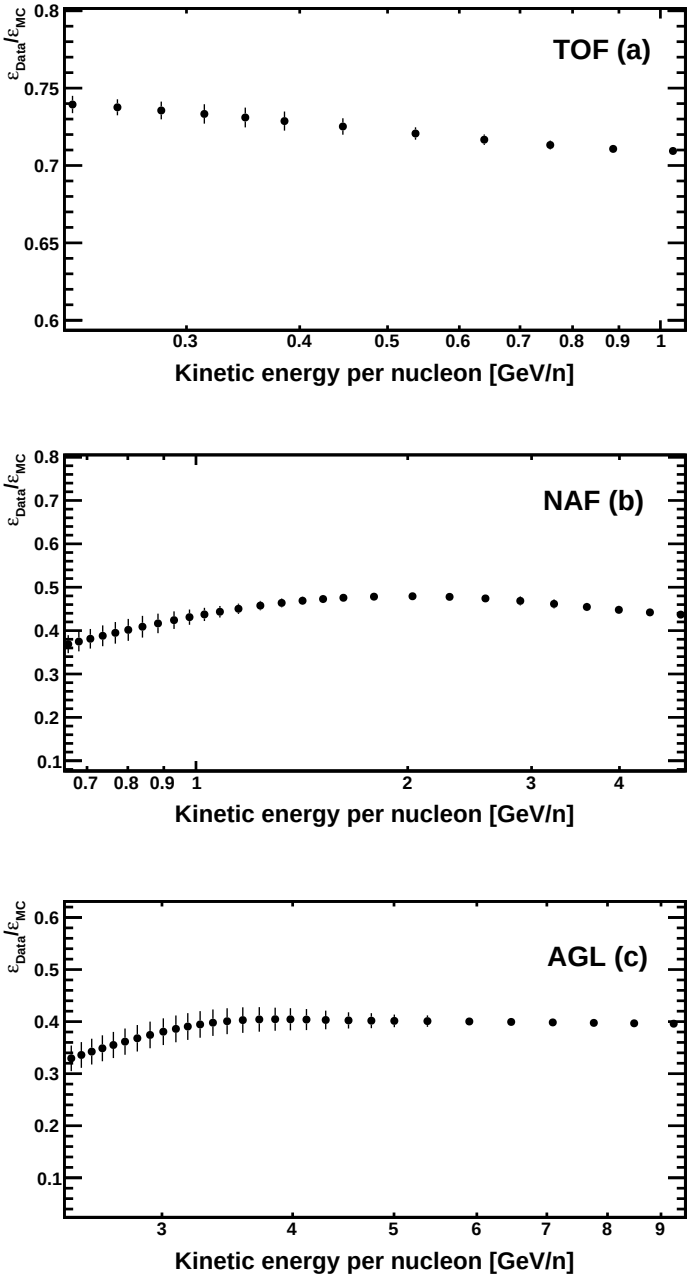

Figure 7.6: Total data/simulations corrections in the TOF (a), NAF (b) and AGL (c) ranges. Uncertainties correspond to the error propagation from each spline used in the calculation.

$$A = \frac{N_{sel}}{N_{gen}} A_{top} \,. \tag{7.11}$$

Figure 7.7 shows the acceptance as a function of the kinetic energy per nucleon for deuterons in the three different velocity ranges, together with the spline fits. The TOF acceptance rises at the lowest energies, eventually reaching a plateau. This effect is related to the energy loss and the incidence angle of the particles: depending on their incidence angle, the amount of material crossed is larger, and they lose more energy, becoming unable to traverse the magnetic field. Both RICH ranges also show a sharp rise of the acceptance in their first bins due to the Cherenkov radiation emission threshold. As the area of the NAF is smaller than the AGL, its geometric acceptance is significantly lower than the one of the AGL.

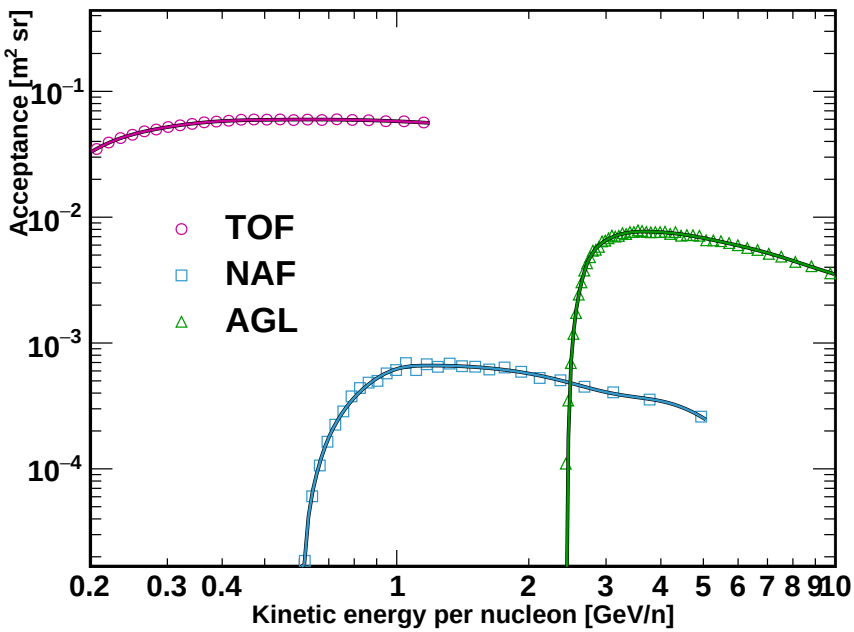

Figure 7.7: Deuteron acceptance as a function of the kinetic energy per nucleon for the TOF (purple circles), NAF (blue squares) and AGL (green triangles), together with the spline fits.

7.6 Event counting

The event counting procedure is described in detail in chapter 5. The event counting is performed in both the proton and the deuteron velocity bins built in section 7.1. In the proton scale, the proton counts are extracted, while in the other the deuterons are counted. Figure 7.8 shows the number of deuterons as a function of the kinetic energy per nucleon for the AGL range, using ten years of AMS-02 data in both the proton and deuteron scales. The sudden changes in the number of events are related to bin width, exposure time and acceptance. It is interesting to notice how the number of events is more larger in the deuteron scale because the geomagnetic cutoff velocity was lower as it was calculated with the rigidity and the deuteron mass.

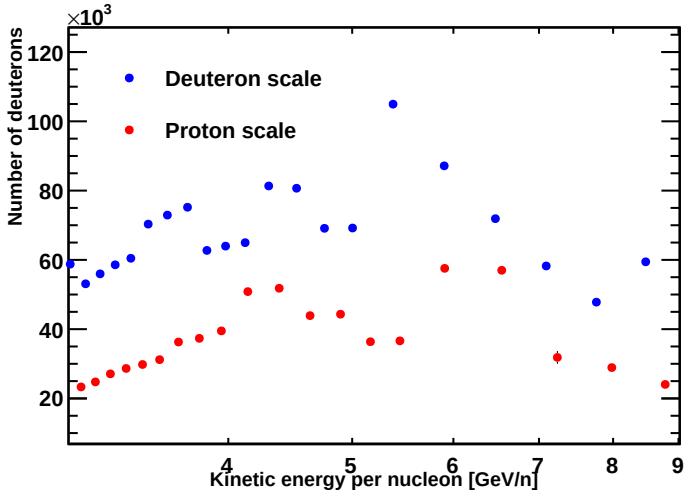

Figure 7.8: Number of deuterons in the AGL range in the deuteron and proton scales.

Once the counts are extracted from the data, as discussed in chapter 6, they must be unfolded together with data/simulation corrections, $\delta(x)$. We then calculate the flux re-writing equation 7.1 as

$$\Phi(x_i) = \frac{\hat{N}(x_i)}{A(x_i)\Delta T \Delta x_i}, \tag{7.12}$$

where $\hat{N}(x_i)$ is the unfolded number of events.

In the next section, the estimation of the uncertainties associated with the measurement of the flux will be presented.

7.7 Systematic uncertainties

In the previous sections, all the necessary terms for the unfolded flux calculation were discussed in detail. However, the assessment of the uncertainties in each bin is necessary to have a complete measurement. In the flux definition given in equation 7.1, the only factor that does not have an associated uncertainty is the bin width defined previously for the measurement. The remaining factors and the unfolding procedure are sources of systematic uncertainties[2].

The methods for obtaining the uncertainties on the number of events and on the unfolding are described in chapters 5 and 6, respectively. The uncertainties on the remaining factors, namely $\delta(x_i)$ and A, are discussed in this chapter.

7.7.1 Acceptance

The acceptance has three sources of uncertainty:

1. **X+C cross-sections:** most of AMS material is carbon [10]. Therefore the interactions that particles may have while traversing the detector in the simulations are subject to the uncertainties in the cross-section models used as input to the simulations. These uncertainties impact the number of events passing the event selection.
2. **Statistical uncertainties:** the finite number of simulated events implies statistical uncertainties to the value of the acceptance in each bin.
3. **Velocity scale:** as seen in figure 7.7, the acceptance has regions where it varies rapidly with the kinetic energy per nucleon. Due to the high slope, the acceptance calculation is affected by the choice of the evaluation point inside each bin.

The AMS-02 collaboration has reported that the p + C inelastic cross sections have an uncertainty of about 10% at 1 GV, reflecting in a 1% uncertainty on the acceptance for protons [9] at the same rigidity. Hence, we used a 1% uncertainty contribution in the proton acceptance in the whole measurement range. In the case of the deuterons, as they have a larger cross section, the uncertainties on the acceptance were estimated to be 2%.

Since a spline is used to have a smooth and continuous description of the acceptance, the statistical uncertainties are not taken bin-by-bin but rather via the impact they have on the spline fit. The uncertainty bands of

[2]The systematics of the exposure time were estimated by varying the geomagnetic cutoff safety factor and were found to be negligible.

the fit, shown in figure 7.7, are used to have a continuous description of the statistical uncertainty.

To calculate the uncertainty related to the choice of the evaluation point of the acceptance, we assume that the bin is a uniform distribution as we could choose any point inside the it. This leads to the uncertainty

$$\sigma_A^2 = \left(\frac{\partial A}{\partial \beta}\right)^2 \sigma_\beta^2 \,, \tag{7.13}$$

where $\partial A/\partial\beta$ is the slope of the acceptance, and σ_β^2 is the variance of a uniform distribution of width $\Delta\beta$, that is $\sigma_\beta = \Delta\beta/\sqrt{12}$. Hence, the larger the change in the acceptance, the larger the error. In the same way, the larger the bin, the larger the error.

7.7.2 Efficiency corrections

Similarly to the acceptance, the first source of uncertainties in the data/simulation corrections is statistical. As it was done for the acceptance, these corrections are also smoothed with spline fits. Therefore, the impact of the statistical uncertainties is assessed via their impact on these fits. Examples of uncertainty bands in each fit are shown in section 7.4. In addition to the statistical error, one must consider that these ratios are obtained as a function of the rigidity and converted to velocity. The tracker resolution is about 10%, and the TOF, NAF and AGL have resolutions of 4%, 0.35%, and 0.12%, respectively. This resolution difference might lead to a mismatch between both scales simply due to resolution effects. Propagating the uncertainty yields the equation

$$\sigma_\delta^2 = \left(\frac{\partial \delta(R)}{\partial R}\right)^2 \sigma_R^2 \,, \tag{7.14}$$

where σ_R is the rigidity resolution. From this equation, it can be seen that regions with flat efficiencies are less penalized by the conversion, as expected. Conversely, in regions where there are more significant variations, the uncertainties are more considerable. Since there are several efficiencies, one per group of selection criteria, the total uncertainty is given by the sum in quadrature of all of them

$$(\sigma_\delta^{tot})^2 = \sum_i (\sigma_\delta^2)_i \,, \tag{7.15}$$

where i is the data/simulation ratio index.

7.7.3 Error breakdown

In order to appreciate how the total error and each of its components evolve, figure 7.9 shows the systematic error breakdown for the measurement of the deuteron flux as a function of the kinetic energy per nucleon for ten years of AMS-02 data for the three different subdetectors. Overall, the total uncertainties are below 10% in the measurement range, dominated mainly by the systematics. The errors associated with the unfolding and acceptance are the most important contributions, reaching their highest values in the first bins of each range. In the case of the NAF and AGL, the explanation is the Cherenkov emission threshold. As the velocity gets closer to this value, fewer events are reconstructed, leading to a sharp drop in the acceptance, which increases the error depending on $\partial A/\partial\beta$. In addition, it means this region of the detector response function is less populated, increasing the uncertainty of the unfolding. In the TOF, the unfolding is the dominant contribution, especially at the lowest energies. This is linked to the energy loss at this region, which produces a significant bias in the detector response function (see chapter 6), and reduces the acceptance significantly, as can be seen in figure 7.7.

7.8 Flux measurement results

7.8.1 Kinetic energy per nucleon

After obtaining the all necessary ingredients for the complete measurement of the fluxes of deuterons and protons, including the systematic uncertainties, the final results can be computed. Figures 7.10a and 7.10b show the unfolded deuteron flux and the deuteron-to-proton flux ratio, respectively, obtained with ten years of AMS-02 data as a function of the kinetic energy per nucleon, between 0.2 and 10 GeV/n, compared to previous experiments [11][12][13][14]. The new measurements provide high-precision data in the previously unexplored region from 4 to 10 GeV/n.

Previous experiments are affected by large systematic uncertainties, while AMS-02 results have percent level precision, providing the first ever data betweem 4 and 10 GeV/n. Note that the data provided by previous experiments have been collected in different time periods, thus being subject to different solar modulation levels. This can explain the apparent tension between experimental results below 4 GeV/n. While AMS-02 data covers almost an entire solar cycle, data from BESS, for instance, were collected during a solar maximum [13].

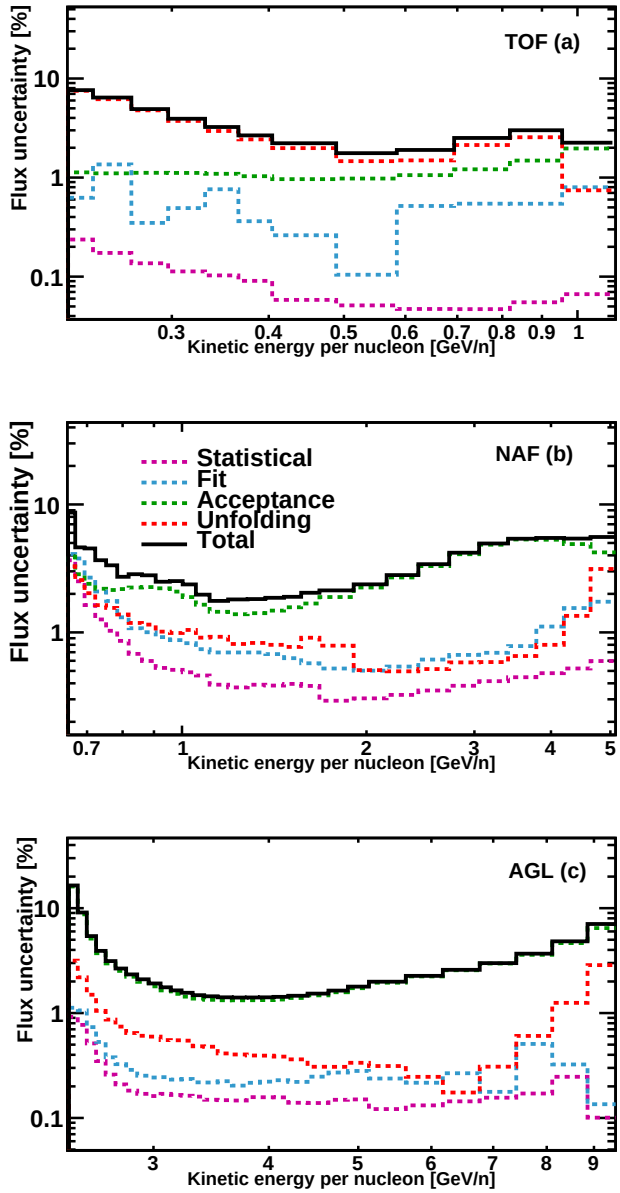

Figure 7.9: Breakdown of the errors of the deuteron flux measurement with 10 years of AMS-02 data. TOF is shown in panel (a), while panels (b) and (c) show the NAF and AGL, respectively. The total uncertainties are represented by the solid black lines, while the colored dashed lines represent each uncertainty component: statistical (purple), fit (light blue), acceptance (green), and unfolding (red).

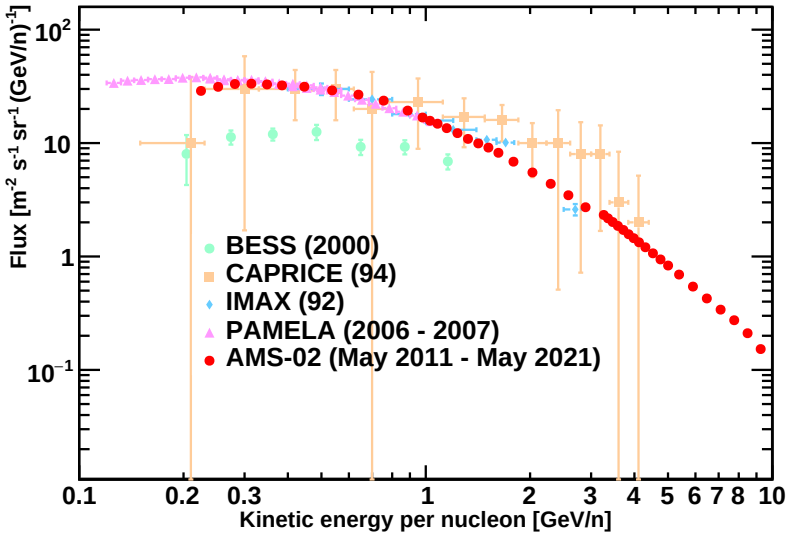

(a)

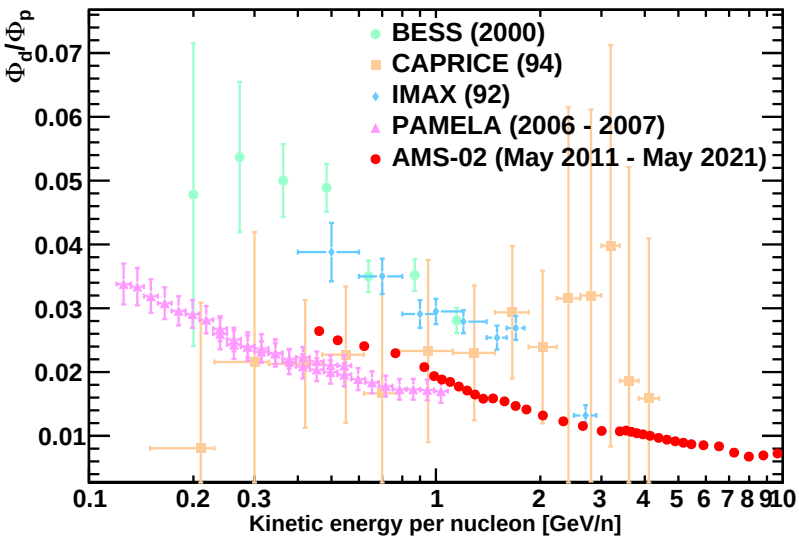

(b)

Figure 7.10: Measured deuteron flux (a) and deuteron-to-proton (b) as a function of the kinetic energy per nucleon compared to previous experiments. The errors shown are the sum in quadrature of statistical and systematic uncertainties. See text for discussion.

7.8.2 Fluxes as a function of rigidity

As explained in section 7.1, the velocity binning was built such that they have a correspondence to the rigidity bins, allowing for the measurement of the fluxes as a function of R using equation 7.1. As all the quantities involved in this calculation were obtained as a function of the velocity, they must be converted for the obtention of the flux as a function of the rigidity. The acceptance, efficiency corrections, and bin width are readily converted. However, the exposure time and event counts require special attention.

As the velocity bins were created to be subdivisions of a rigidity bin, the event counts as a function of R are given by

$$N(R_i) = \sum_{\beta_j \in R_i} N(\beta_j)\,, \tag{7.16}$$

that is, they are the sum of the counts in all velocity bins, β_j, that belong to that given rigidity bin, R_i.

Due to the cumulative nature of the exposure time, its conversion to rigidity is not given by the sum of all the exposure times, but rather by the maximum exposure time as a function of the velocity in that given rigidity bin. That is

$$T(R_i) = max(T(\beta_j)),\ \beta_j \in R_i\,. \tag{7.17}$$

Figure 7.11a shows the proton and deuteron fluxes as a function of the rigidity measured with ten years of AMS-02 data. It is important to recall that the difference in the rigidity ranges of both measurements is due to the separation of isotopes in velocity bins, which leads to different momentum ranges due to the mass difference between the particles. The differences in the behavior of both fluxes are seen in figure 7.11b, where the deuteron-to-proton flux ratio is shown, displaying a flat behavior above 3 GV. A more detailed interpretation of this result will be given in section 7.9.

In order to validate the presented results, the results were compared to the $Z = 1$ flux published by the AMS-02 collaboration in [1]. The published flux does not have any distinction between protons and deuterons. Hence, to properly compare it to the results obtained in this thesis, we must use the sum of the proton and deuteron fluxes, that is, $\Phi_{p+d} = \Phi_p + \Phi_d$. In addition, to avoid discrepancies coming from solar modulation, the fluxes of both protons and deuterons used in the comparison were measured

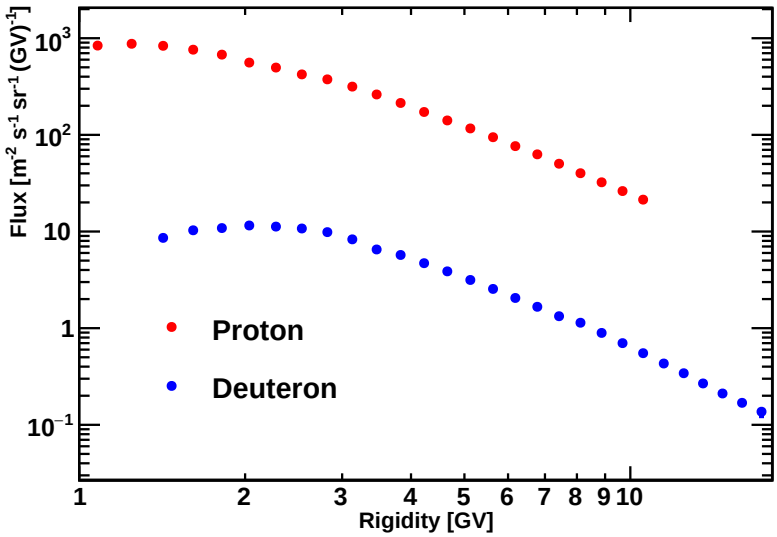

(a)

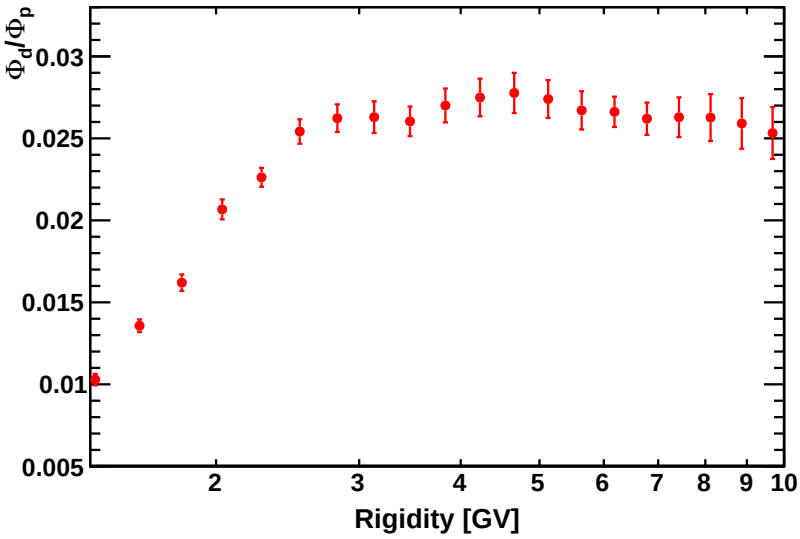

(b)

Figure 7.11: Measured deuteron and proton fluxes (a) and deuteron-to-proton flux ratio (b) as a function of the rigidity. The errors shown are the sum in quadrature of statistical and systematic uncertainties. See text for discussion.

with 7 years of AMS-02 data, from May 2011 to May 2018, the same data sample used in the proton flux publication [1].

The normalized residuals between the measurements are shown in figure 7.12. The agreement between the fluxes is better than 5% in the entire rigidity range. This agreement supports the methodology for measuring the isotopic fluxes developed in this thesis.

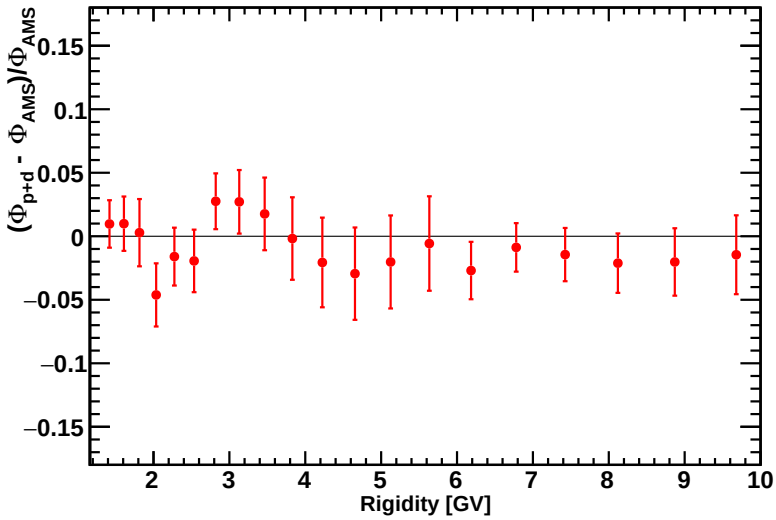

Figure 7.12: Comparison between the published AMS-02 $Z = 1$ flux and the proton plus deuteron flux measured in this work with seven years of data. The uncertainties correspond to the error propagation of the total uncertainties of each measurement.

7.9 Interpretation

As shown in figure 1.7 of chapter 1, the main progenitors of deuterons in CRs are protons, ^{3}He, ^{4}He, and heavier nuclei. Protons and ^{3}He have higher contributions at low energies, amounting to about 40% of the deuteron production at 1 GeV/n. ^{4}He and heavier nuclei, are the dominant channels at higher energies, contributing to $\approx$ 60% and $\approx$ 40% of the deuteron production and 10 GeV/n, respectively. While protons and ^{4}He are mostly primary, ^{3}He is a secondary species. Using the results obtained in this thesis, combined with the fluxes of helium isotopes published by AMS-02 [5], we can compute the secondary-to-primary ratios d/p and d/^{4}He, and the secondary-to-secondary ratio d/^{3}He. To avoid introducing biases in

the calculation of the d/^{4}He and d/^{3}He ratios due to the solar modulation, the deuteron flux was measured using the same period of data as the publication, from May 2011 to November 2017. These ratios, together with the deuteron flux, were then compared to the prediction of the SLIM model tuned to the AMS-02 Li/C, Be/C, B/C, and F/Si data in chapter 3, using the updated cross-section set OPT12up22 presented in chapter 2. The results are shown in the top panels of figures 7.13 and 7.14. The comparison with the deuteron flux shows two different regimes. Below 2 GV, the model undershoots the data by about 40%, as indicated by the data/model ratio shown in the figure. This behavior at the lowest rigidities could be explained by the parametrization of the source spectrum. As discussed in [15], a simple power-law, as we used in these calculations, is able to reproduce the data of carbon and oxygen above 7 GV. Below this value, the model deviates from the data, especially for hydrogen and helium. This could be solved by the use of a double power law but requires a more detailed analysis that will not be discussed here. Above 3 GV, we note that the constant fit to the data/model ratio shows that the model overestimates the deuteron flux by an approximately constant factor $\approx 20\%$. Remarkably, a similar offset value is obtained in comparing the model and the flux ratios. Since the offset is constant, the propagation parameters obtained from the (Li, Be, B)/C analysis can reproduce well the shape of these flux ratios of lighter nuclei. The difference in normalization caused by the deuteron over-production is most likely linked to the deuteron production cross-sections. As discussed before the main channels of deuteron production are ^{4}He and heavier nuclei, such as oxygen. The uncertainties associated with the relevant cross sections are known to be large [16], which could explain this behavior. It is also worth noting that the peak seen around 3 GV in the flux ratios is linked to the proton fusion channel, which is relevant at lower energies as mentioned before. These results indicate that the correct interpretation of the new data provided by AMS-02 will require a study of the relevant cross sections.

7.10 Conclusion

The measurement of the fluxes of $Z = 1$ isotopes in cosmic rays provides valuable data for constraining propagation models and testing their universality concerning A/Z. Thanks to the precise measurements of the velocity and momentum of its subdetectors, AMS-02 can provide the measurements of the deuteron flux and deuteron-to-proton flux ratio in an uncharted energy range, and measure the same quantities as a function

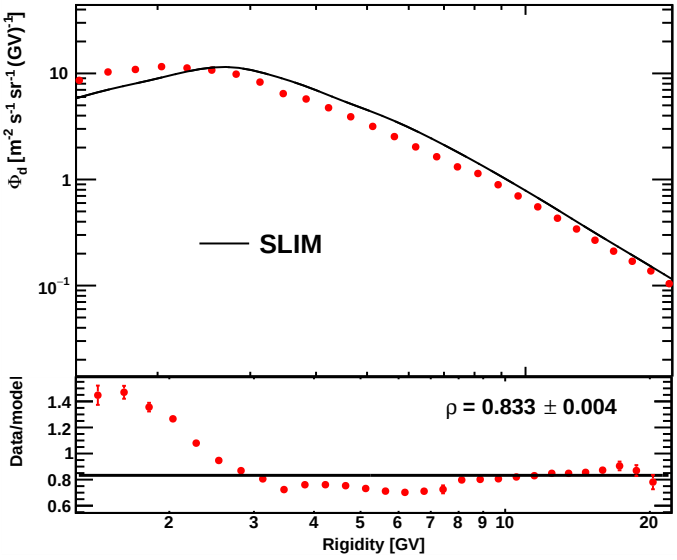

(a)

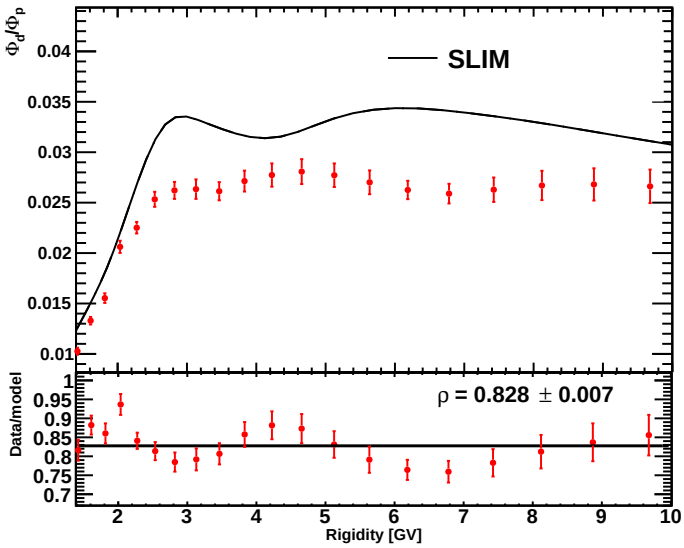

(b)

Figure 7.13: The deuteron flux (a) and the deuteron-to-proton flux ratio (b) compared to the SLIM model. The bottom panels of each figure show the ratio between the re-scaled model (factor ρ fitted) and the data.

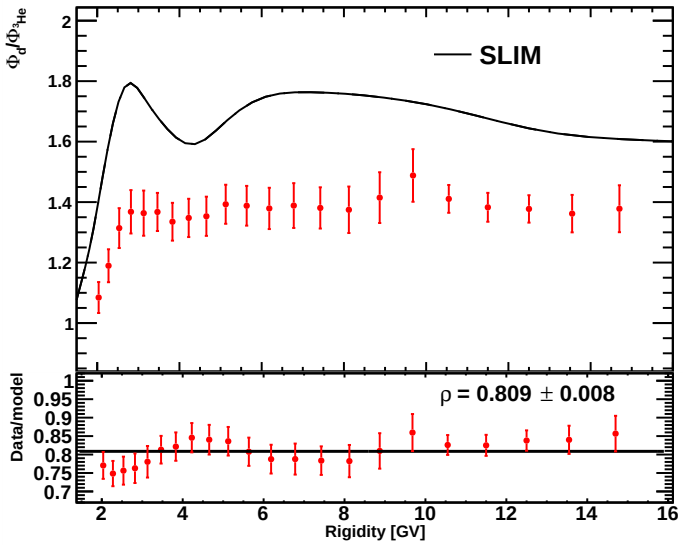

(a)

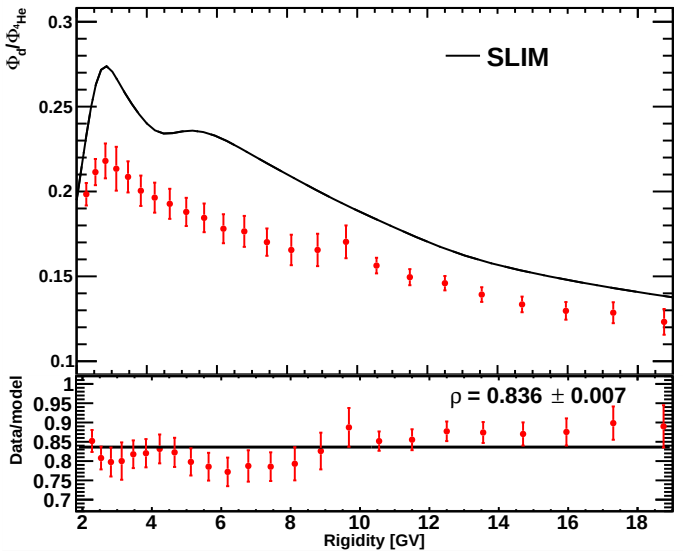

(b)

Figure 7.14: The d/^{3}He (a) and the d/^{4}He flux ratios (b) compared to the SLIM model. The bottom panels of each figure show the ratio between the re-scaled model (factor ρ fitted) and the data.

of the rigidity for the first time. In this chapter, we used the methods developed in the second part of this thesis to obtain these measurements. The particularities of the isotopic analysis were treated from the beginning. First, the velocity binning was defined to allow for the measurement of the fluxes as a function of the rigidity, taking into account the different masses of the isotopes. The implications of this choice on calculating the exposure time were discussed, leading to the obtention of two different exposure times, one for each isotope. The event selection and the efficiencies and data/simulation corrections were presented, followed by the calculation of acceptance obtained for each particle. The errors associated with the measurement were also presented, indicating that the systematics are dominant in all ranges, with the acceptance and unfolding being the most relevant in the three velocity ranges, leading to total uncertainties between 2 and 8% in the interval of the measurement. The resulting fluxes extended the current range of measurements of the deuteron flux and deuteron-to-proton flux ratio up to 10 GeV/n. For the first time, the isotopic fluxes of single-charged particles have been measured as a function of rigidity. The analysis was validated by comparing the sum of the isotopic fluxes with the $Z = 1$ flux published by the AMS-02 collaboration, showing an agreement better than 5% for all points.

The relevant secondary-to-primary and secondary-to-secondary ratios were calculated and compared, together with the deuteron flux, to the SLIM model tuned to heavier nuclei data from AMS-02 in chapters 2 and 3. The comparison has shown that the model is overestimates the deuteron flux above 3 GV by a factor of 20%, which is also seen in the flux ratios. The discrepancy is in line with the typical uncertainties on the measurements of the relevant nuclear cross sections, reinforcing that a thorough analysis of the available data is necessary before interpreting the AMS-02 results.

Appendix 7.A Trigger logic

The AMS-02 trigger logic was developed to make fast and reliable decisions about the quality of a given event. It uses information from the TOF, ACC and ECAL, which are then processed in a dedicated electronics board [17]. In order to optimize the live time of the detector, a tree architecture was adopted with two different stages: only if the first conditions are met, the second is evaluated.

The first stage is the Fast Trigger (FT), which starts if certain conditions are met in the TOF or the ECAL. In the case of the TOF, the digital signals from the paddles in each plane are used to check whether the signal is

Sub-trigger	TOF signal	ECAL signal	ACC signal
Single charge	4/4 planes, MT	any	no signal
Normal ions	4/4 planes, HT	any	<5 hits
Slow ions	4/4 planes, HT	any	<5 hits
Electrons	4/4 planes, MT	deposited energy above threshold in both coordinates	any
Photons	any	same as Electrons, but with ECAL shower axis inside AMS acceptance	any
Unbiased charged	3/4 planes, MT	any	any
Unbiased electromagnetic	any	deposited energy above threshold in one of the coordinates	any

Table 7.5: Sub-trigers used for data acquisition in the LVL1 trigger of AMS-02 [18][17].

above a medium (MT) or high (HT) threshold. The ECAL uses the signals on x or y super-layers, requiring a minimum number of cells above a given threshold. If the FT has a signal, the data acquisition system is set to busy for 1μs, and the next stage of the trigger is evaluated.

The second stage, Level 1 (LVL1), combines information from the TOF, ECAL and ACC to create five sub-triggers with different physics goals and two unbiased sub-triggers used to evaluate the efficiency of some subdetectors and of the physical trigger itself. Based on what is presented on [18], table 7.5 summarizes these sub-triggers.

Appendix 7.B Trigger efficiency

The efficiency of the trigger in a given analysis depends on the selection criteria applied to the sample. Events that pass through all the tracker layers, for instance, are less likely to have hits in the ACC and therefore are cleaner, implying a higher efficiency. Conversely, events which are only required to pass through the inner tracker and layer 1 can have a higher inclination, leading to the rejection of more events by the trigger logic.

In order to estimate the trigger efficiency, a reference sample is created by applying the selection criteria of the analysis and only requiring unbiased trigger signals. The selected sample requires at least one of the physical sub-triggers. This process was done for the three velocity ranges in experimental data. The results are shown in figure 7.15. The higher efficiency of the

NAF compared to the TOF and AGL is precisely due to the central geometry of its events.

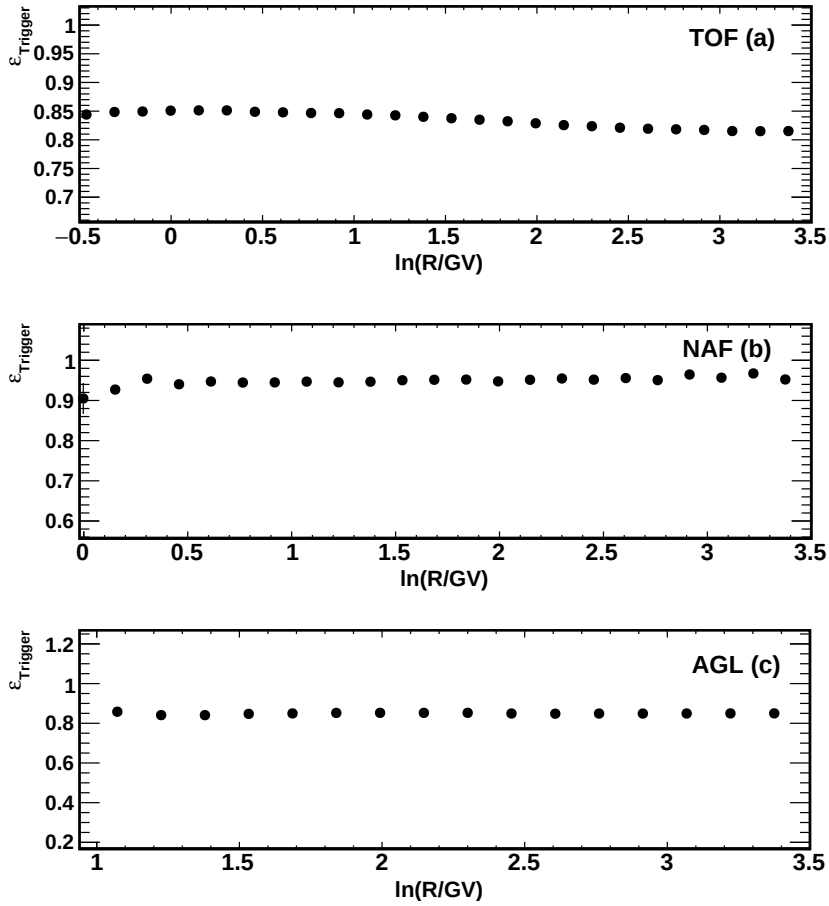

Figure 7.15: Trigger efficiency in data for $Z = 1$ particles as a function of $ln(R)$ for in the TOF (a), NAF (b) and AGL (c).

Bibliography

[1] M. Aguilar et al. The alpha magnetic spectrometer (ams) on the international space station: Part ii — results from the first seven years. *Physics Reports*, 894:1–116, 2021. ISSN 0370-1573. doi: https://doi.org/10.1016/j.physrep.2020.09.003. URL https://www.sciencedirect.com/science/article/pii/S0370157320303434. The Alpha Magnetic Spectrometer (AMS) on the International Space Station: Part II - Results from the First Seven Years.

[2] V. Bindi et al. Calibration and performance of the AMS-02 time of flight detector in space. *Nuclear Instruments and Methods in Physics Research Section A: Accelerators, Spectrometers, Detectors and Associated Equipment*, 743:22–29, 2014. ISSN 0168-9002. doi: https://doi.org/10.1016/j.nima.2014.01.002. URL https://www.sciencedirect.com/science/article/pii/S0168900214000102.

[3] F. Giovacchini, J. Casaus, and A. Oliva. The AMS-02 RICH detector: Status and physics results. *Nuclear Instruments and Methods in Physics Research Section A: Accelerators, Spectrometers, Detectors and Associated Equipment*, 952:161797, February 2020. doi: 10.1016/j.nima.2019.01.024. URL https://doi.org/10.1016/j.nima.2019.01.024.

[4] Marius Potgieter. Solar modulation of cosmic rays. *Living Reviews in Solar Physics*, 10, 2013. doi: 10.12942/lrsp-2013-3. URL https://doi.org/10.12942%2Flrsp-2013-3.

[5] M. Aguilar et al. Properties of Cosmic Helium Isotopes Measured by the Alpha Magnetic Spectrometer. *Phys. Rev. Lett.*, 123:181102, Nov 2019. doi: 10.1103/PhysRevLett.123.181102. URL https://link.aps.org/doi/10.1103/PhysRevLett.123.181102.

[6] D.F. Smart and M.A. Shea. A review of geomagnetic cutoff rigidities for Earth-orbiting spacecraft. *Advances in Space Research*, 36(10):2012–2020, 2005.

[7] C. Stormer. The polar aurora. *Quarterly Journal of the Royal Meteorological Society*, 82(351):115–115. doi/abs/10.1002/qj.49708235123. doi: 10.1002/qj.49708235123.

[8] C. C. Finlay et al. International Geomagnetic Reference Field: the eleventh generation. *Geophysical Journal International*, 183(3):1216–1230, October 2010. doi: 10.1111/j.1365-246x.2010.04804.x. URL https://doi.org/10.1111/j.1365-246x.2010.04804.x.

[9] M. Aguilar et al. Precision Measurement of the Proton Flux in Primary Cosmic Rays from Rigidity 1 GV to 1.8 TV with the Alpha Magnetic

Spectrometer on the International Space Station. *Phys. Rev. Lett.*, 114:171103, Apr 2015. doi: 10.1103/PhysRevLett.114.171103. URL https://link.aps.org/doi/10.1103/PhysRevLett.114.171103.

[10] Q. Yan, V. Choutko, A. Oliva, and M. Paniccia. Measurements of nuclear interaction cross sections with the alpha magnetic spectrometer on the international space station. *Nuclear Physics A*, 996:121712, 2020. ISSN 0375-9474. doi: https://doi.org/10.1016/j.nuclphysa.2020.121712. URL https://www.sciencedirect.com/science/article/pii/S0375947420300221.

[11] O. Adriani et al. Measurements of cosmic-ray hydrogen and helium isotopes with the PAMELA experiment. 818(1):68, feb 2016. doi: 10.3847/0004-637x/818/1/68. URL https://doi.org/10.3847/0004-637x/818/1/68.

[12] G. A. de Nolfo et al. A measurement of cosmic ray deuterium from 0.5–2.9 GeV/nucleon. *AIP Conference Proceedings*, 528(1):425–428, 2000. doi: 10.1063/1.1324352. URL https://aip.scitation.org/doi/abs/10.1063/1.1324352.

[13] K.C. Kim et al. Cosmic ray 2H/1H ratio measured from BESS in 2000 during solar maximum. *Advances in Space Research*, 51(2):234–237, 2013. ISSN 0273-1177. doi: https://doi.org/10.1016/j.asr.2012.01.015. URL https://www.sciencedirect.com/science/article/pii/S0273117712000567. The Origins of Cosmic Rays: Resolving Hess's Century-Old Puzzle.

[14] P. Papini et al. High-energy deuteron measurement with the CAPRICE98 experiment. *Astrophys. J.*, 615:259–274, 2004. doi: 10.1086/424027.

[15] Mathieu Boudaud, Yoann Génolini, Laurent Derome, et al. AMS-02 antiprotons' consistency with a secondary astrophysical origin. *Phys. Rev. Research*, 2:023022, Apr 2020. doi: 10.1103/PhysRevResearch.2.023022. URL https://link.aps.org/doi/10.1103/PhysRevResearch.2.023022.

[16] B. Coste et al. Constraining Galactic cosmic-ray parameters with $Z \leqslant 2$ nuclei. *A&A*, 539:A88, 2012. doi: 10.1051/0004-6361/201117927. URL https://doi.org/10.1051/0004-6361/201117927.

[17] M. Duranti. Measurement of the atmospheric muon flux on ground with the AMS-02 detector, 2012. 153 p. Ph. D. Thesis (Physics) - Università degli Studi di Perugia, Perugia, 2012.

[18] M. Behlmann. Measurement of Helium Isotopic Composition in Cosmic Rays with AMS-02, 2018. 145 p. Ph. D. Thesis (Physics) - Massachusetts Institute of Technology (MIT), 2018.